Journal of Advanced Ceramics
2024, **13**(12): 1985–1995
https://doi.org/10.26599/JAC.2024.9220991

Research Article

Phase engineering on high-entropy transition metal dichalcogenides and the entropy-enhanced thermoelectric performance

Hongxiang Chen[1,2,3,4,✉], Enhui Zhao[1], Xiaochun Wen[1,3], Sheng Liu[1], Shiyu Li[1], Jiantao Fu[1], Hengzhong Fan[2,✉], Bing Xiao[5,✉], Yongsheng Zhang[2]

[1] *School of Materials Science and Engineering, Fujian University of Technology, Fuzhou 350118, China*
[2] *State Key Laboratory of Solid Lubrication, Lanzhou Institute of Chemical Physics, Chinese Academy of Sciences, Lanzhou 730000, China*
[3] *Fujian Provincial Key Laboratory of Advanced Materials Processing and Application, Fuzhou 350118, China*
[4] *State Key Laboratory of Structural Chemistry, Fujian Institute of Research on the Structure of Matter, Chinese Academy of Sciences, Fuzhou 350002, China*
[5] *State Key Laboratory of Electrical Insulation and Power Equipment, School of Electrical Engineering, Xi'an Jiaotong University, Xi'an 710049, China*

Received: June 30, 2024; Revised: October 16, 2024; Accepted: October 18, 2024

Abstract: High-entropy structures in layered compounds, especially transitional metal dichalcogenides (TMDCs), have powered the field with disordered and versatile chemical compositions, showing great potential in various functional applications, including energy storage and catalysis. However, the reported high-entropy phases are mainly 1T phases, 2H phases are rare, and approximately 3R phases are still lacking. Here, phase engineering of high-entropy TMDCs is achieved by tuning the chemical composition of $(Mo_{0.5}W_{0.5})_{1-x}(Nb_{0.5}Ta_{0.5})_xSe_{2+\delta}$, $0 \le x < 1$, and $-0.1 \le \delta \le 0.3$. A phase diagram is constructed to guide the synthesis of pure 2H/3R phases over a wide composition/entropy range. The increase in VB-group element content and Se overdose facilitated the formation of 3R phases, whereas the opposite occurred for 2H phases. Thermodynamic first-principles calculations evaluate the stability of phases in different polytypes and compositions, matching well with the composition-dependent crystalline habits. Moreover, the optimized thermoelectric performance, with a figure of merit (zT = 0.36@723 K) in 2H phase of x = 0.2, is attributed to the low thermal conductivity (κ) caused by the high-entropy effect, which is one of the highest among (Mo/W)Se_2-based materials. Our work enriches high-entropy TMDCs with versatile polytypes, expanding their potential uses for various fields.

Keywords: high-entropy; layered compounds; crystal structure; thermoelectric; entropy engineering; phase engineering

1 Introduction

Transitional metal dichalcogenides (TMDCs), a series of classical layered compounds, have been studied extensively in various fields [1–3]. The chemical composition can be written as TX_2, where T is the transition metal, and X is the chalcogen element S/Se/Te. The van der Waals connection between the layered slabs, which contributes to their unique mechanical properties, can be exfoliated to monolayered or few-layered forms [4]. Moreover, their tunable bandgap [1,5] and versatile quantum effects [6–8] make them promising for applications [9,10] in optoelectronics, thermoelectrics, catalysis, etc.

Recently, the use of high-entropy van der Waals compounds [11–14], including chalcogenides, phosphide chalcogenides, and halides, has increased, with great potential in functional materials and low-dimensional physics. Owing to the rich elemental combination choices, more than 20 high-entropy phases have been reported in TMDCs [15]. Moreover, owing to the weak bonding in van der Waals gaps, the intercalation of high-entropy metals can be realized as a new form of high-entropy layered compounds [12]. However, most of the reported high-entropy TMDCs are in 1T phase, and only a few high-entropy 2H phases have been reported [13,16]. Thus, the rule of phase formation has not been clarified. Different polytypes have significantly different physical properties [17] because of differences in their crystal and electronic structures. Unlike 1T and 2H phases, 3R phase lacks inversion symmetry, which is applicable for information storage [18], second-order-harmonic generation [19], and piezoelectricity [20]. Until now, the high-entropy 3R phase has not been realized. Exploring high-entropy TMDCs in different polytypes will significantly enrich high-entropy systems and expand their applications in new fields, including optical-electronic, catalysis, piezoelectric, and superconductivity. Moreover, entropy/phase engineering has been proven to improve thermoelectric performance [21–25], and more attention should be given to high-entropy TMDCs.

In this work, we synthesized a series of middle-/high-entropy layered compounds with the formula $(Mo_{0.5}W_{0.5})_{1-x}(Nb_{0.5}Ta_{0.5})_xSe_2$. By tuning the chalcogen atmosphere during high-temperature synthesis and the relative ratio between VB- and VIB-group elements, the controllable synthesis of high-entropy 2H/3R phases over a wide composition range can be realized. A phase diagram was built as a function of the nominal Se content and the

✉ Corresponding authors.
E-mail: H. Chen, hungxchen@163.com;
H. Fan, hzhfan@licp.cas.cn;
B. Xiao, bingxiao84@xjtu.edu.cn

composition of the metal atomic sites. The thermodynamic parameters are calculated theoretically to reveal the formation mechanism. Introducing VB-group elements into (Mo/W)Se_2-based compounds results in more carriers and changes the lattice disorder and configuration entropy. By characterizing the thermoelectric properties, the effect of doping on the electrical and thermal conductivities was investigated. With increasing x, the thermal conductivity (κ) increased, whereas the temperature dependence decreased. The optimized thermoelectric performance, with a dimensionless figure of merit (zT = 0.36@ 723 K), was found when x = 0.2 for the in-plane case. This value is one of the highest among TMDCs, and the superior performance can be attributed to the low thermal conductivity caused by the enhanced configuration entropy. Our work provides a series of high-entropy TMDCs with rich polytypes, including 2H and 3R phases, with improved thermoelectric properties, possibly promising candidates for flexible thermoelectric devices and other multifunctional uses.

2 Experiment and methods

2.1 Synthesis methods

$(Mo_{0.5}W_{0.5})_{1-x}(Nb_{0.5}Ta_{0.5})_xSe_{2+\delta}$ (x = 0–1, δ = −0.1–0.3) samples were synthesized via the solid-state synthesis method. High-purity Mo (99.99%, Aladdin, China), W (99.99%, Aladdin, China), Nb (99.99%, Aladdin, China), Ta (99.99%, Aladdin, China), and Se (99.99%, Aladdin, China) powder were weighed at nominal chemical ratios. After being ground carefully, the mixed powder was sealed in a quartz tube under high vacuum. The silica tubes were heated to 1373 K for 12 h and then held at that temperature for 48 h. Targeting phases were obtained in powder form after cooling to room temperature within 24 h. The as-prepared powder samples were ground and sieved with 300 mesh for spark plasma sintering (SPS) for 10 min at 1173 K at a uniaxial pressure of 45 MPa via the commercial equipment (SPS-5T-5-III, Shanghai Chenhua Science and Technology Co., Ltd., China). The relative density of the samples was measured via the Archimedes method. SPS-sintered bulk samples were cut into rectangular bars (3 mm × 3 mm × 10 mm) and rectangular/circular plates with thicknesses of approximately 1.5 mm for electrical and thermal transport measurements, respectively. The sizes of SPS-sintered samples were ϕ12.5 mm × 15 mm, which allowed two sets of samples to be cut with the basal plane perpendicular/parallel to the pressing direction.

2.2 Phase analyses

The phase compositions of the end products were characterized by an X-ray diffractometer (XRD; D8 Advance, Bruker, Germany) using Cu Kα radiation (Cu Kα1: 1.5406 Å, Kα2: 1.5444 Å). XRD data were collected from 5° to 95° in steps of 0.02°. The morphology and chemical composition were detected through a field emission scanning electron microscope (FESEM; NovaNano EM450, FEI, USA) equipped with an energy-dispersive spectrometer (EDS; Model Link-Isis, Oxford, UK). High-angle annular dark field (HAADF) images, selected area electron diffraction (SAED), and EDS mapping analysis were collected via a transmission electron microscope (TEM; Tecnai G^2 F20, FEI, USA) operated at 200 kV with a highly efficient (4 quadrant) energy dispersive X-ray system.

2.3 Thermoelectric property characterizations

Seebeck coefficient (S) and electrical conductivity (σ) at high temperatures were measured via CTA-3s (Beijing Cryoall, China). Thermal diffusion coefficient (D) measurements were conducted by a laser thermal conductivity meter (LFA 457A, Netzsch, Germany) in an argon atmosphere in $\kappa = D \cdot C_p \cdot \rho$. in which the specific heat (C_p) was estimated from the Dulong–Petit value. The sample density (ρ) was measured via the Archimedes drainage method. Hall coefficient (R_H) was measured with a Hall effect test system (NYMS-II, Shanghai Nengyi, China) via the van der Pauw method under a reversible magnetic field of 1.5 T. Carrier concentration (p_H) and carrier mobility (μ_H) were calculated as $p_H = 1/(e \cdot R_H)$ and $\mu_H = \sigma/(p_H \cdot e)$. The uncertainties in the measurements of σ, S, κ, and R_H were estimated to be ±3%, ±5%, ±7%, and ±5%, respectively.

2.4 Theoretical calculations

All first-principles calculations based on density functional theory (DFT) were performed via three-dimensional (3D) periodic boundary conditions and the projected augmented wave (PAW) method, as available in the VASP software package [26,27]. Regarding the valence shells of all relevant elements, we included $4p^6 4d^5 5s^1$ (Mo), $5d^4 6s^2$ (W), $4p^6 4d^4 5s^1$ (Nb), $5d^3 6s^2$ (Ta), and $4s^2 4p^4$ (Se). For plane wave expansion in reciprocal space, the kinetic energy cutoff value was set to 400 eV for the structural optimizations and total energy calculations of $(Mo_{0.5}W_{0.5})_x(Nb_{0.5}Ta_{0.5})_{1-x}Se_2$ high-entropy transition metal dichalcogenides. The exchange-correlation effects of electrons were calculated via generalized gradient approximation (GGA) in terms of Perdew–Burke–Ernzerhof (PBE) density functional [28]. For counting the van der Waals interactions among the atomic layers in bulk transition metal dichalcogenides, the standard PBE+D3 method was employed in all the calculations [29]. k-mesh used in the energy calculations for the supercell models was 4 × 1 × 1, as generated by Γ-point centered scheme in the Brillouin zone. The total energy and the mean atomic force were 1.0×10^{-6} eV/cell and 0.01 eV/Å, respectively.

3 Results and discussion

3.1 Phase engineering

TMDCs have various polytypes [1,5,30]. Inside the layered slabs, the metal atomic layers are sandwiched by two chalcogen element layers, with each metal atom surrounded by six chalcogen atoms. Generally, two kinds of coordination conditions exist in TMDCs: octahedral and trigonal prismatic coordination, as shown in Figs. 1(a) and 1(b), respectively. Figures 1(c)–1(e) show the three most common polytypes, including 1T, 2H, and 3R phases with multiple principal metal elements; the former number indicates the number of layered slabs in the unit cell, and the latter capital letter indicates the crystal system of the compound [31]. Figure 1(f) shows the hexagonal atomic arrangement in each metal layer. Here, we designed a series of entropy engineering samples with a metal element combination of MoWNbTa, in which the mole ratios of Mo : W and Nb : Ta were fixed at 1 : 1. The ratio between VIB-group elements (MoW) and VB-group elements (NbTa) was tuned, modulating the mixing configuration entropy (ΔS_{mix}), as shown in Fig. 1(g), as calculated by $\Delta S_{mix} = R \cdot \sum_N^{i=1} c_i \ln c_i$, where c_i is the atomic fraction of the ith metal element, R is the gas constant, and N is the total number of metal elements [32]. ΔS_{mix} reached a maximum of 1.39R when x = 0.5 with equimolar metal elements.

Here, the solid-state synthesis method was applied to obtain the target phases, with the elemental powder used as raw materials.

Chalcogen elements (X) melt at relatively low temperatures and then react with metal elements (T), forming TX_3 phases. With increasing temperature, TX_3 decomposes, and TX_2 forms. The chalcogen elements exist in both the vapor and solid states at high temperatures. Therefore, the content of the chalcogen affects the synthesis atmosphere at high temperatures, influencing the crystallization and the thermodynamic stability of different polytypes [33]. Therefore, the content of the chalcogen element Se was adjusted, and the obtained samples were characterized via XRD.

The effect of the nominal chalcogen content was studied via phase analysis of selected samples with varying δ values from −0.1 to 0.3, as shown in Fig. 2, and the whole XRD patterns are given in Fig. S1 in the Electronic Supplementary Material (ESM). The red-heart and black-blade symbols in Figs. 2–4 indicate the (103) peak of 2H phase and the (104) and (015) peaks of 3R phases, which are commonly used to identify 2H and 3R polytypes [34,35]. When the nominal Se content was 1.9 with a 5% deficiency, the characteristic peak of (103) peak did not shift but was significantly broader than that at $\delta = 0$. Similar broadening phenomena were also observed for samples with different x values. The obvious peak broadening phenomena indicate the introduction of more stacking or in-plane disorder due to the deficiency of Se. Moreover, we found that Se deficiency is beneficial for forming the 2H phase, as demonstrated by Figs. 2(b) and 2(c), which are in almost pure 2H phases and a 2H/3R mixed phase, respectively.

When $x = 0.2$, as revealed by the characteristic (103) peak in Fig. 2(a), the as-prepared samples are all in 2H phase, suggesting that the Gibbs free energy of the 2H phase is more negative than that of the 3R phase ($\Delta G_{2H} < \Delta G_{3R}$). An increase in Se content results in sharper diffraction peaks, suggesting an improvement in the crystallinity. As shown in Fig. 2(b), in samples with $x = 0.3$, 3R and 2H phases existed when $\delta \geq 0$. When $\delta = 0$, (103) peak of 2H phase was greater than (104) and (015) peaks, whereas when Se content increased, the diffraction peaks of 3R phase became more significant. When δ increased to 0.3, the content of 2H phase decreased substantially. These results suggest that excessive Se is

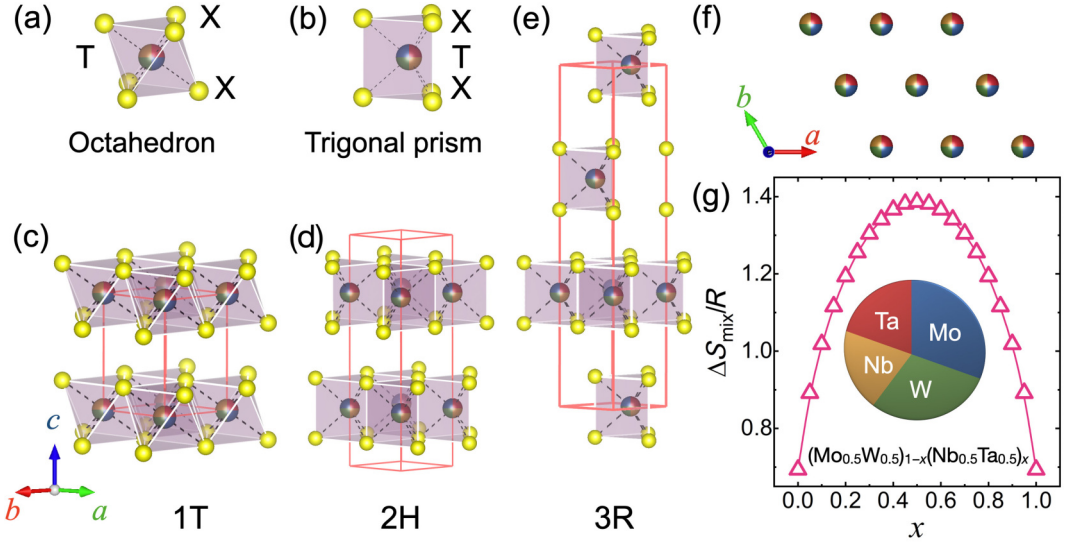

Fig. 1 Structural design of high-entropy TMDCs: (a) octahedral coordination and (b) trigonal prismatic coordination. Crystal structure of (c) 1T phase, (d) 2H phase, and (e) 3R phase. (f) Hexagonal arrangement of a single layer of metal atoms. (g) Composition dependence x of mixing configuration entropy of metal atom sites with $(Mo_{0.5}W_{0.5})_{1-x}(Nb_{0.5}Ta_{0.5})_x$, $0 < x < 1$. The multicolored and yellow balls indicate the metal and chalcogen atoms, respectively.

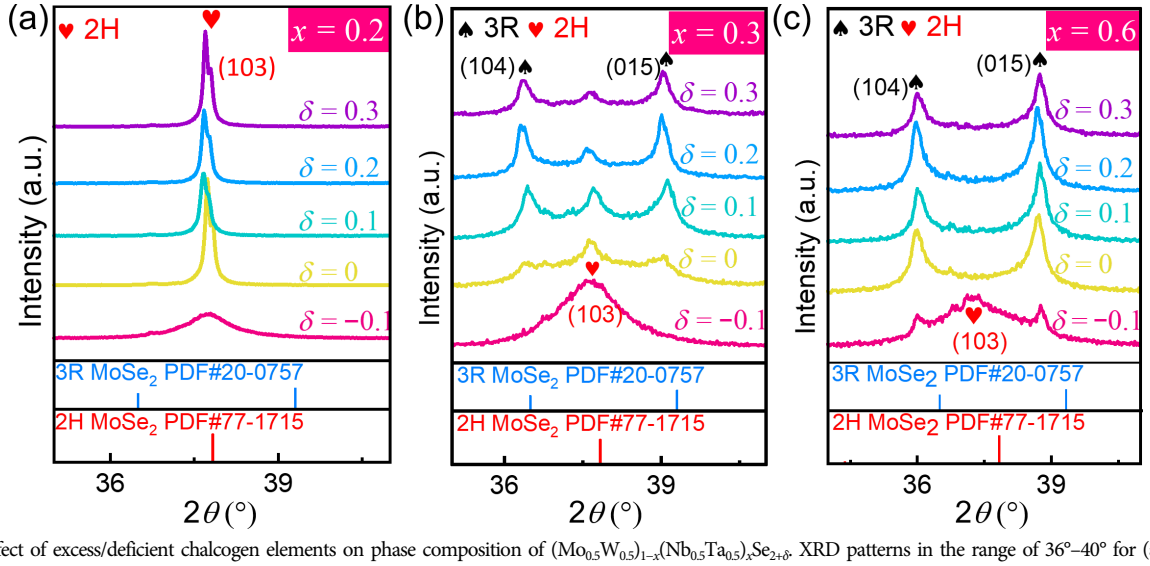

Fig. 2 Effect of excess/deficient chalcogen elements on phase composition of $(Mo_{0.5}W_{0.5})_{1-x}(Nb_{0.5}Ta_{0.5})_xSe_{2+\delta}$. XRD patterns in the range of 36°–40° for (a) $x = 0.2$, (b) $x = 0.3$, and (c) $x = 0.6$. Characteristic peaks of 2H phase and 3R phase are marked by red heart and black blades, respectively.

beneficial for improving crystallinity and facilitating the formation of 3R phase at the synthesis temperature.

The chemical composition of metal elements affects the valence electron concentration, which plays a pivotal role in the thermal stability of polytypes [36–39]. Here, a series of compounds with varying x values and excess Se content δ = 0.2 were prepared. (002)/(003) peak of 2H/3R phases shifted to lower angles, as shown in Fig. 3(a), with increasing x. The characteristic peaks of 2H and 3R phases shifted to higher angles with increasing NbTa content, as shown in Fig. 3(b).

As shown in Figs. 3(a) and 3(b), when $x \le 0.2$, the samples are in pure 2H phases, and the lattice parameters a and c increased and decreased with increasing x, respectively. When x increased to 0.3, the product was composed of mixed 2H and 3R phases. The mixed phases are in different polytypes but should have the same chemical composition, as demonstrated by the high overlap of (002) peak of 2H phase and (003) peak of 3R phase. Pure 3R phases were obtained when $0.4 \le x \le 0.7$, in which (104) and (105) peaks of 3R phase were observed, and (103) peak of 2H phase was absent. When $x \ge 0.8$, splitting peaks at approximately 14° and various peaks at 35°–40° suggest that the end product was in complex composite phases in different polytypes and deviated chemical compositions.

XRD patterns in the measured ranges of the samples in Fig. 3 are given in Fig. S2 in the ESM. After indexing and refining the lattice parameters of XRD patterns, the evolution of the lattice parameters with x content is shown in Fig. 3(c). Here, c/2 of 2H and c/3 of 3R phases were given to demonstrate the spacing change between layered slabs. As shown in Fig. 3(c), when $x \le 0.3$, the layer spacing (c/2 of the 2H phase) decreased relatively sharply from 6.4795(5) Å when x = 0 to 6.3774(13) Å when x = 0.3. For 2H and 3R phases, the layer spacing and a value are very close. However, the decreasing tendency of the layer spacing (c/2 of 3R phase) was significantly reduced when $x \ge 0.3$. The in-plane lattice parameter a exhibits the opposite trend, decreasing almost linearly as x value increases. The unit-cell volume (Fig. S3 in the ESM) also increases with increasing x, suggesting that the average ionic radius of Nb+Ta is larger than that of Mo+W.

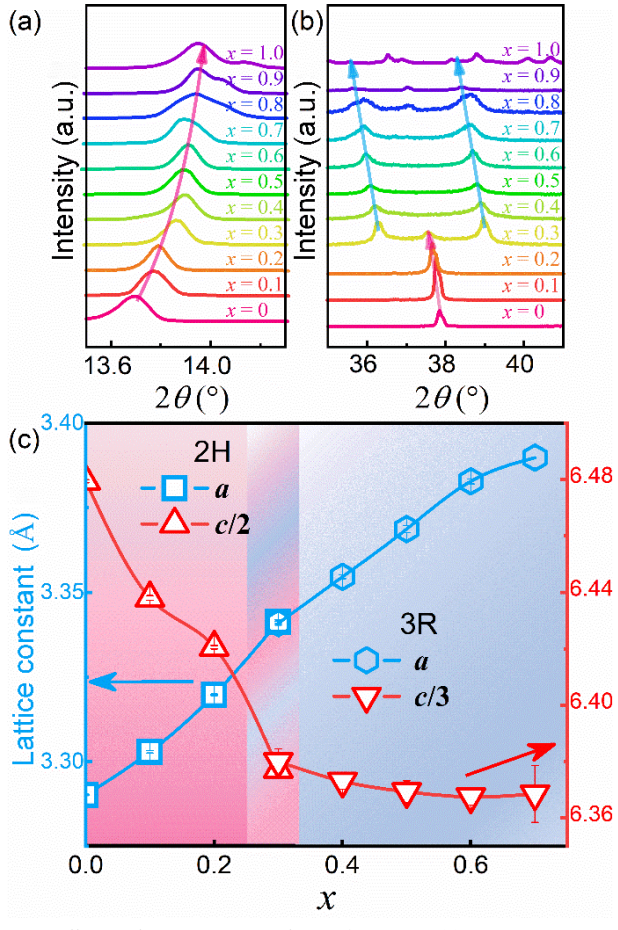

Fig. 3 Effects of composition of metal atoms. (a) XRD spectra of $(Mo_{0.5}W_{0.5})_{1-x}(Nb_{0.5}Ta_{0.5})_xSe_{2.2}$. (b) Magnification of characteristic peaks. (c) Blue line is cell parameter a, and red line is cell parameter c. Arrows in (a) and (b) suggest that peak position shifts with increasing x.

In addition to XRD, electron microscopy was also effective in identifying the polymorphs of TMDCs [40–42]. Therefore, HAADF images of 2H phase and 3R phase were collected and are shown in Figs. 4(a) and 4(b). Fast Fourier transform (FFT) results of the two samples are in the same period. When x = 0.2, only a trigonal pattern was detected, suggesting the arrangement of the single metal atomic layer. However, when x = 0.7, the atomic arrangement is more complicated; more atoms from different atomic layers can be observed to match well with the structure of 3R phase [41]. Moreover, elemental mapping analyses were performed on selected regions for both samples, as shown in Figs. 4(c) and 4(d), to demonstrate homogeneity. Each element is homogeneously distributed in the as-prepared samples.

A phase diagram was built by summarizing the phase analysis results of samples with varying x and δ. As shown in Fig. 5, for samples with $x \le 0.2$, the end products are all in 2H phases. Moreover, when $\delta = -0.1$, the samples with $x \le 0.6$ are in pure 2H phases. 3R phases can be obtained for compositions in the orange-colored region of Fig. 5, $0.4 \le x \le 0.7$ and $0 \le \delta \le 0.3$. For samples with $x \ge 0.8$, it is difficult to obtain a single phase.

3.2 Thermodynamics and electronic structures

Moreover, thermodynamics and electronic structure calculations were performed to reveal the formation mechanism and evolution of the electronic structures. As shown in Fig. 6(a), for $MoSe_2$ and WS_2, formation enthalpy (ΔH) of 1T phase is much greater than that of 2H and 3R phases. However, for $NbSe_2$ and $TaSe_2$, the difference became much weaker, which is consistent with the existence of all three polytypes. ΔH values of $NbSe_2$ and $TaSe_2$ are more negative than those of $MoSe_2$ and $TaSe_2$ are, suggesting that the doping of Nb/Ta in $(Mo/W)Se_2$ is thermodynamically favored. As shown in Fig. 6(b), with increasing NbTa content, the Gibbs free energy became more negative, and the difference between 1T and 2H/3R phases decreased, which could account for the difficulty in synthesizing a single phase with x > 0.8. As shown in Fig. 6(c), the difference between 2H and 3R phases ($\Delta G_{3R} - \Delta G_{2H}$) is positive when x = 0 and 0.1, indicating that 2H phase is preferred. When x = 0.3 or 0.4, the difference between 2H and 3R phases is negligible, accounting for the coexistence of both phases experimentally when x = 0.3. However, for samples with higher x values, 3R phases are favored.

Regarding the electronic structures, total density of states (TDOS) results suggest that 2H and 3R phases of $MoSe_2$ and WSe_2 are semiconductors with a bandgap of 0.3 eV, which is usually underestimated in the theoretical results. The thermodynamically unfavored 1T phases are metallic with a nonzero TDOS at the Fermi level. The doping of Nb or Ta will cause an increase in TDOS, which is 0.218 and 0.314 meV/f.u. when x = 0.4 and 0.8, respectively, suggesting the carrier doping effect by Nb/Ta and the resulting metallic electronic structures. Moreover, as shown in Fig. 6(d), TDOS curves of all the

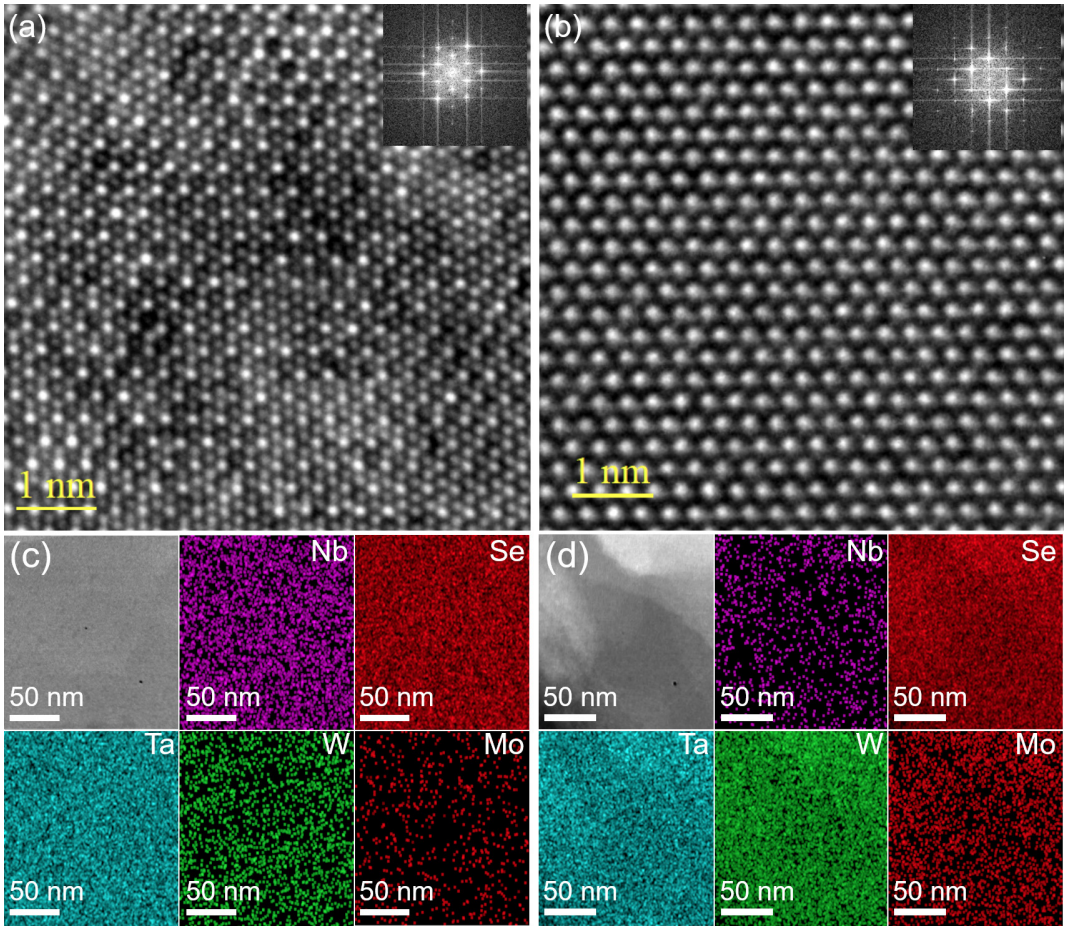

Fig. 4 HAADF images and EDS mapping results of 3R and 2H phases with $\delta = 0.2$. HAADF images of (a) 3R-phase sample with $x = 0.7$ and (b) 2H-phase sample with $x = 0.2$. FFT results of HAADF images are given in insets of (a) and (b). Elemental mappings of samples with (c) $x = 0.7$ and (d) $x = 0.2$.

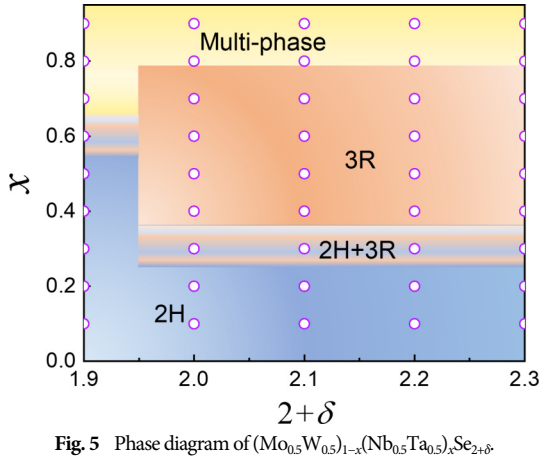

Fig. 5 Phase diagram of $(Mo_{0.5}W_{0.5})_{1-x}(Nb_{0.5}Ta_{0.5})_xSe_{2+\delta}$.

compositions almost completely overlap around the Fermi level, indicating similar electronic properties in 2H and 3R phases.

3.3 Thermoelectric properties

Owing to their quasi two-dimensional structure, TMDCs hold a promising future for flexible thermoelectric devices [43]. The thermoelectric properties of samples with $x \leq 0.7$ were characterized systematically via SPS-sintered samples with a relative density higher than 90%. When VIB-group elements occupy the metal atomic sites, the di-selenides are in semiconducting states, with a bandgap of approximately 1.2 eV [44]. For samples with $0.1 \leq x \leq 0.7$, the resistivity increased with increasing temperature, indicating metallic electrical transport behavior, as shown in Figs. 7(a) and 7(c), for currents flowing in the in-plane and cross-plane directions, respectively. The sample cutting schemes and the current directions are shown in the insets of Figs. 7(b) and 7(e). As shown in Fig. S4 in the ESM, a preferred stacking of layered polycrystals along the pressing direction was observed.

$(Mo_{0.5}W_{0.5})_{1-x}(Nb_{0.5}Ta_{0.5})_xSe_2$ can be regarded as a doping of $(Mo_{0.5}W_{0.5})Se_2$ by VB-group elements (NbTa) in the content of x. As shown in Fig. 1(g), ΔS_{mix} was modulated by the x value in a dome-like form and reached a maximum when $x = 0.5$. VB-group di-selenides are usually in metallic states accompanied by various kinds of charge density wave transitions [5]. Therefore, increasing the number of VB-group elements will dismiss the bandgap and introduce more carriers, which is consistent with TDOS results in Fig. 6(d). The composition-dependent in-plane resistivities $\rho_{\parallel}$ at 310 and 800 K are shown in Fig. 7(b). When $x \leq 0.3$ and $T = 310$ K, $\rho_{\parallel}$ decreased significantly from 21.6 μΩ·m for $x = 0.1$ to 10.7 μΩ·m for $x = 0.3$. When x value further increased, the resistivity increased and reached a maximum when $x = 0.5$, which is also the maximum of ΔS_{mix}. The increase in $\rho_{\parallel}$ can be attributed to the Anderson localization [11] of carriers caused by the strong disorder introduced by the relatively high ΔS_{mix}. Therefore, even though the carrier number increased, the resistivity still increased because of the decreased mobility.

Moreover, when the applied current flows in the cross-plane direction, the as-determined cross-plane resistivity $\rho_{\perp}$ is much greater than $\rho_{\parallel}$, which is 610.6 μΩ·m at 310 K and 860.6 μΩ·m at 800 K. As shown in Fig. 7(d), all samples exhibited metallic

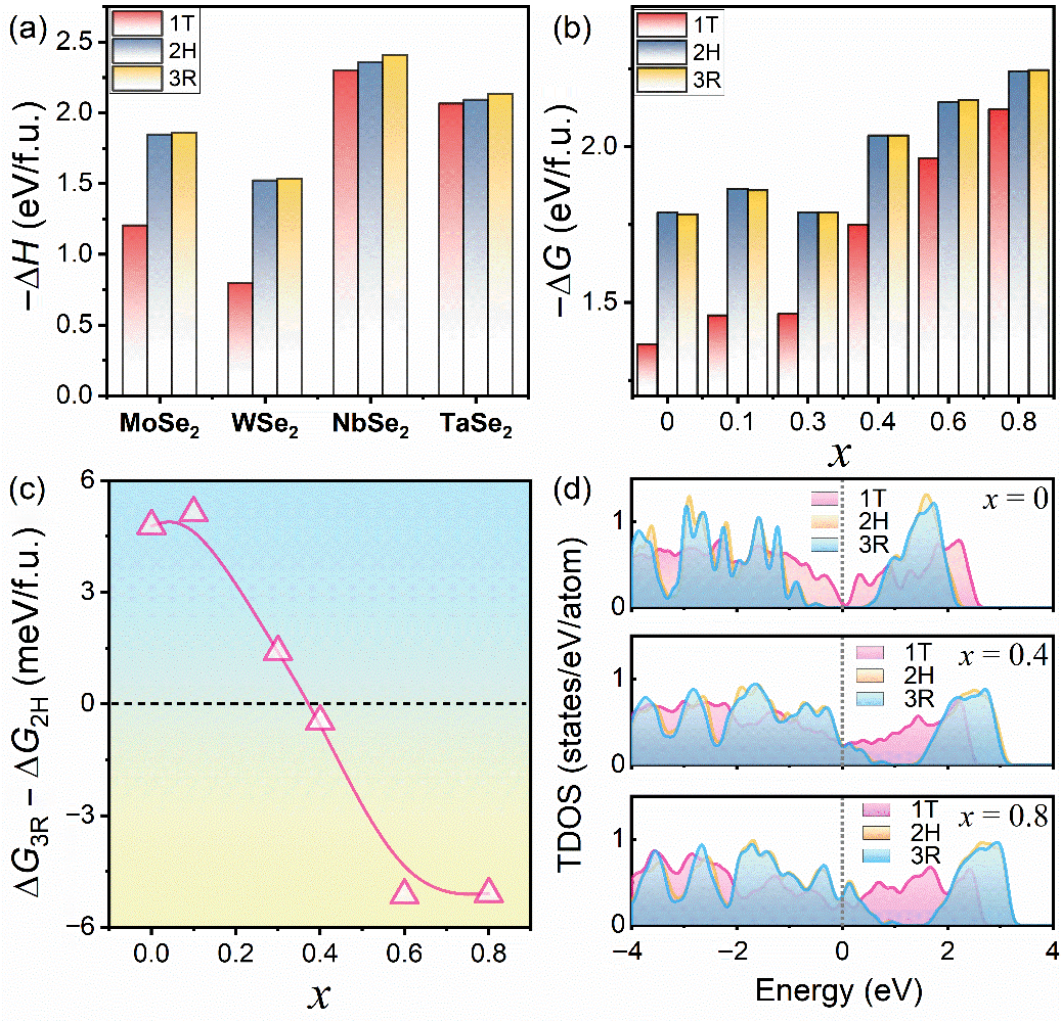

Fig. 6 Thermodynamics and electronic calculations. (a) Formation enthalpy of binary selenides. (b) Gibbs free energy of $(Mo_{0.5}W_{0.5})_{1-x}(Nb_{0.5}Ta_{0.5})_xSe_2$ formation in different polytypes and x values. (c) Gibbs free energy difference between 2H and 3R phases. (d) TDOSs of $x = 0$, 0.4, and 0.8 for different polytypes.

behavior. An increase in x significantly reduced $\rho_\perp$; when $x \geq 0.3$, the resistivity was lower than 1/10 of that at $x = 0.1$. In contrast to the peak-shaped tendency, as observed in Fig. 7(b), the resistivity fluctuated approximately 50 μΩ·m@310 K, as observed in $\rho_\perp$ when $x \geq 0.3$, as shown in Fig. 7(e). The difference between x-dependence of $\rho_\perp$ and $\rho_\parallel$ can be attributed to the Anderson localization effect of $\rho_\perp$, which was less significant than that of $\rho_\parallel$. Moreover, the electrical resistivity anisotropy was evaluated by $\rho_\perp/\rho_\parallel$, as shown in Fig. 7(c). $\rho_\perp/\rho_\parallel$ was ~40 when $x = 0.1$ and reached a minimum of 4.04 when $x = 0.5$.

The carrier concentration and mobility of the as-prepared samples are shown in Fig. 7(f). With increasing x, the carrier concentration increased from 1.9×10^{21} cm^2@$x = 0.1$ to 6.75×10^{22} cm^2 @$x = 0.7$, suggesting that more carriers were introduced with increasing NbTa content. The carrier mobility was low because of the relatively high carrier concentration, which ranged from 1.04 to 2.48 m^2/(V·S). The minimum (1.04 cm^2/(V·S)) mobility was found when $x = 0.5$, with the highest ΔS_{mix}.

Seebeck coefficient was measured during the resistivity measurements. In contrast to the significant anisotropy of resistivity, the difference between the in-plane and cross-plane Seebeck coefficients is relatively small, as shown in Figs. 8(a) and 8(c). For all the samples, $S_\perp$ and $S_\parallel$ increased almost linearly with increasing temperature. As shown in Fig. 8(b), the in-plane Seebeck coefficient $S_\parallel$ decreased from 40 μV/K@310 K and 100 μV/K@800 K to −0.82 μV/K@310 K and 6.67 μV/K@800 K. For the cross-plane case, the tendency was similar. When $x \leq 0.5$, the Seebeck coefficients were positive, suggesting the presence of mainly hole-type carriers. When $x > 0.5$, the Seebeck coefficient became negative, suggesting that the main carrier type became electrons. As shown in Fig. 8(d), $S_\perp$ decreased to −14.4 μV/K.

Entropy engineering has been proven effective in modulating thermal conductivity and thermoelectric performance [45–48]. Here, the thermal conductivity was characterized by heat transport along the in-plane direction ($\kappa_\parallel$) and cross-plane direction ($\kappa_\perp$), as shown in Figs. 9(a) and 9(b), respectively. In the electrical transport case, as shown in Fig. 7, we have illustrated the competition between the increase in carrier amount and the enhanced disorder effect as the doping content of VB group elements increased. For the heat transport case, a similar competitive relationship was found. The total thermal conductivity usually comprises electrical (κ_{ele}) and lattice contributions (κ_{lat}), $\kappa_{total} = \kappa_{ele} + \kappa_{lat}$. In the in-plane cases, the lowest thermal conductivity was observed when $x = 0.2$. The heat transport along the cross-direction is more difficult, the cross-plane $\kappa_\parallel$ values are lower than $\kappa_\parallel$ values are, and the lowest $\kappa_\perp$ value is observed at $x = 0.3$, which is 0.51 W/(m·K)@300 K and 0.43 W/(m·K). Owing to the increased electrical contribution with increasing NbTa content, the lowest values were not detected in the samples with the highest configuration entropy. The lowest

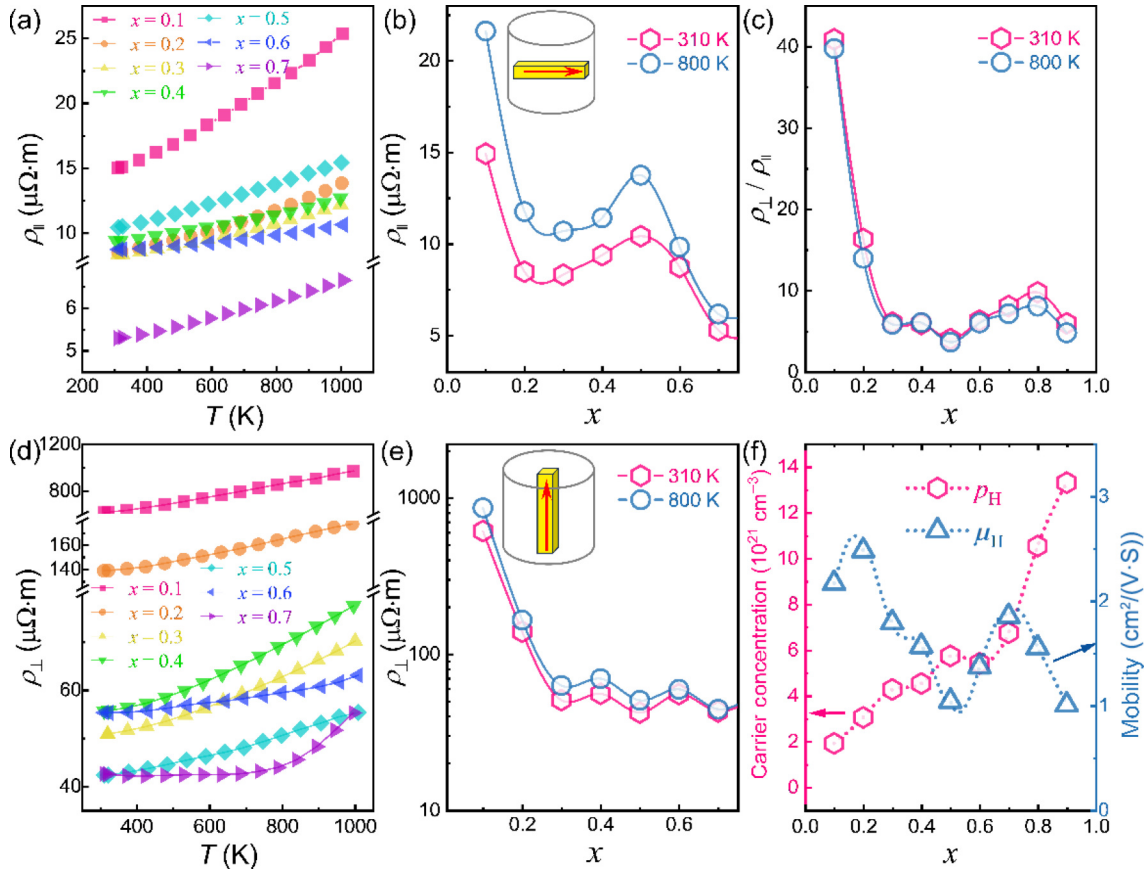

Fig. 7 Electrical transport properties. Temperature-dependent (a) in-plane resistivity $\rho_{\parallel}$ and (d) cross-plane resistivity ($\rho_{\perp}$). Composition dependence of (b) $\rho_{\parallel}$ and (e) $\rho_{\perp}$, (c) resistivity anisotropy factor ($\rho_{\perp}/\rho_{\parallel}$), and (f) p_H and μ_H measured in in-plane cases.

thermal conductivity can be reached by balancing the enhancement of electrical contribution and the reduction of lattice contribution. With increasing x, the temperature dependence decreased, as shown in Figs. 9(a) and 9(b). When x = 0.7, the temperature dependence of $\kappa_{\perp}$ became very weak, as revealed by the flat purple curve in Fig. 9(b).

To evaluate the overall effects of doping on the thermal conductivity, the average thermal conductivity was calculated as $\kappa_{ave} = (2\kappa_{\parallel} + \kappa_{\perp})/3$. The composition dependence of κ_{ave} at 310, 473, and 673 K is shown in Fig. 9(c). With increasing x, κ_{ave} first decreased but then tended to increase. The temperature dependence of κ_{ave} was demonstrated by the gap between different temperatures, as shown by the painted zones in Fig. 9(c). The gap size decreased with increasing x, suggesting that the temperature dependence was reduced, in which the gap was almost closed when x = 0.6.

The electronic component κ_{ele} can be correlated with the electrical conductivity via the Wiedemann–Franz law, which can be calculated by $\kappa_{ele} = L\sigma T$, where $\sigma = 1/\rho$ is the electrical conductivity, T is the absolute temperature, and L is the Lorentz number, whose value can be evaluated via Eq. (1) [49]:

$$L = 1.5 + \exp(-|S|/116) \times 10^{-8} \ (\mathrm{W \cdot \Omega / K^2}) \quad (1)$$

where S is the Seebeck coefficient.

The as-evaluated electrical thermal conductivities of all the samples are given in Figs. S6(a) and S6(b) in the ESM. Usually, the lattice component can be obtained by $\kappa_{lat} = \kappa_{total} - L\sigma T$, as shown in Figs. S6(c) and S6(d) in the ESM. However, the as-obtained lattice component was underestimated, and the electrical component was overestimated, as revealed by the negative values at high temperatures in several samples, as shown in Fig. S6(c) in the ESM. The negative value may be due to the complex band structure or the strong correlation effects in these high-entropy low-dimensional materials.

The power factor, PF = $S^2\sigma$, is given in Fig. S7 in the ESM. PFs of samples with x = 0.1 and 0.2 are close and are the highest among all samples, PF ≈ 0.1 and 0.3 mW·m/K²@723 K. The dimensionless figure of merit, zT = PF·T/κ_{total}, as a function of temperature is shown in Figs. 10(a) and 10(b). At high temperatures, a relatively high in-plane zT was observed in Fig. 10(a), which is much stronger than the cross-plane zT (Fig. 10(b)), which can be attributed to the significant electrical conductivity anisotropy.

The thermoelectric properties of (Mo/W)Se_2 without carrier doping are usually poor, with the highest reported value being $zT \approx 0.016$ in WSe_2 [50]. Previous studies have demonstrated that minor doping by VB-group elements significantly improves their thermoelectric performance, in which the doping content is usually less than 0.1. Interestingly, the best performance in our high-entropy materials was achieved by a relatively high doping content (x = 0.2), in which zT = 0.36@723 K for in-plane case, which is higher than zT = 0.24@723 K of x = 0.1. The higher zT should be attributed to the phonon scattering enhanced by the higher ΔS_{mix}, which suppresses the increase in the electronic component, resulting in a lower κ_{tot} at x = 0.2 than at x = 0.1.

We collected zT values at approximately 723 K for (Mo/W)Se_2-based compounds [50–59] with optimized doping contents, as shown in Fig. 10(c). The vertical and parallel symbols indicate the in-plane and cross-plane cases, respectively. Compared with the thermoelectric properties of other (Mo/W)Se_2-based compounds,

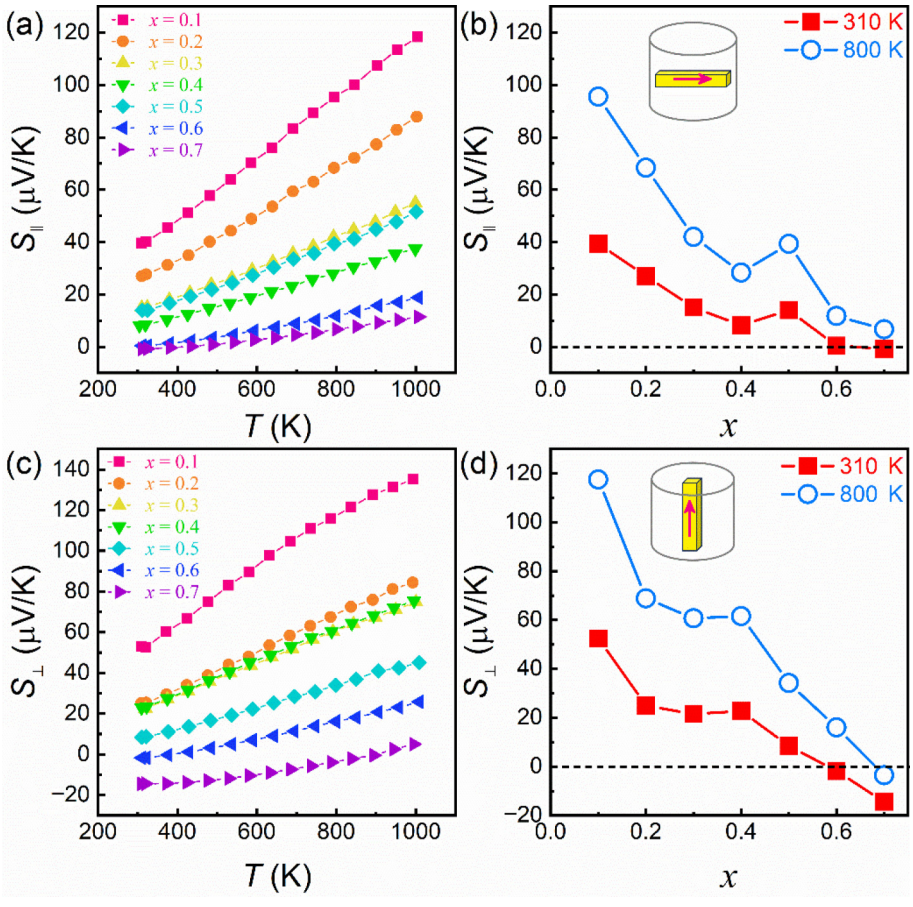

Fig. 8 Seebeck coefficient anisotropy. Temperature-dependent (a) in-plane and (c) cross-plane Seebeck coefficients. Composition-dependent (b) in-plane and (d) cross-plane Seebeck coefficients.

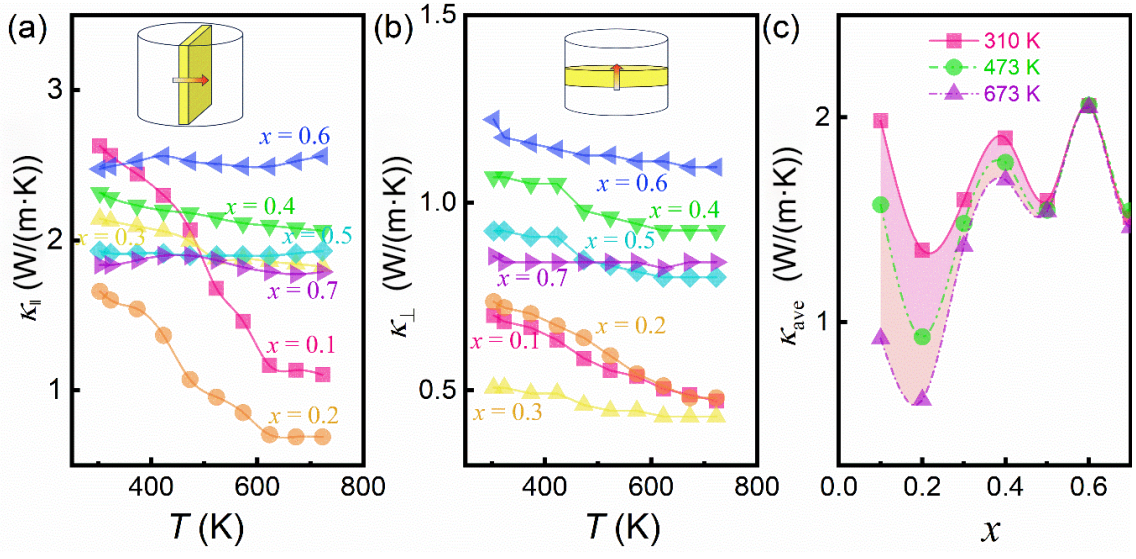

Fig. 9 Thermal conductivity anisotropy. Temperature dependence of (a) in-plane and (b) cross-plane thermal conductivity. (c) Composition dependence of average thermal conductivity at selected temperatures.

zT value of $Mo_{0.4}W_{0.4}Nb_{0.1}Ta_{0.1}Se_2$ (x = 0.2) is the highest. As shown in Fig. 10(c), further doping the chalcogen sites improved zT. Moreover, as demonstrated by the comparison of the corresponding thermal conductivities in Fig. 10(d), the decrease in thermal conductivity plays a pivotal role in improving zT. Our results demonstrated that the high-entropy scheme at the metal atomic site effectively improved the thermoelectric performance to a higher level. Here, a wide-range phase diagram with corresponding thermal electric performances is given, while the optimization of thermoelectric performance requires fine-tuning of the carrier concentration. The as-discovered high-entropy phases possess great potential, as their performance could be improved by fine-tuning the x value and further doping the chalcogen sites.

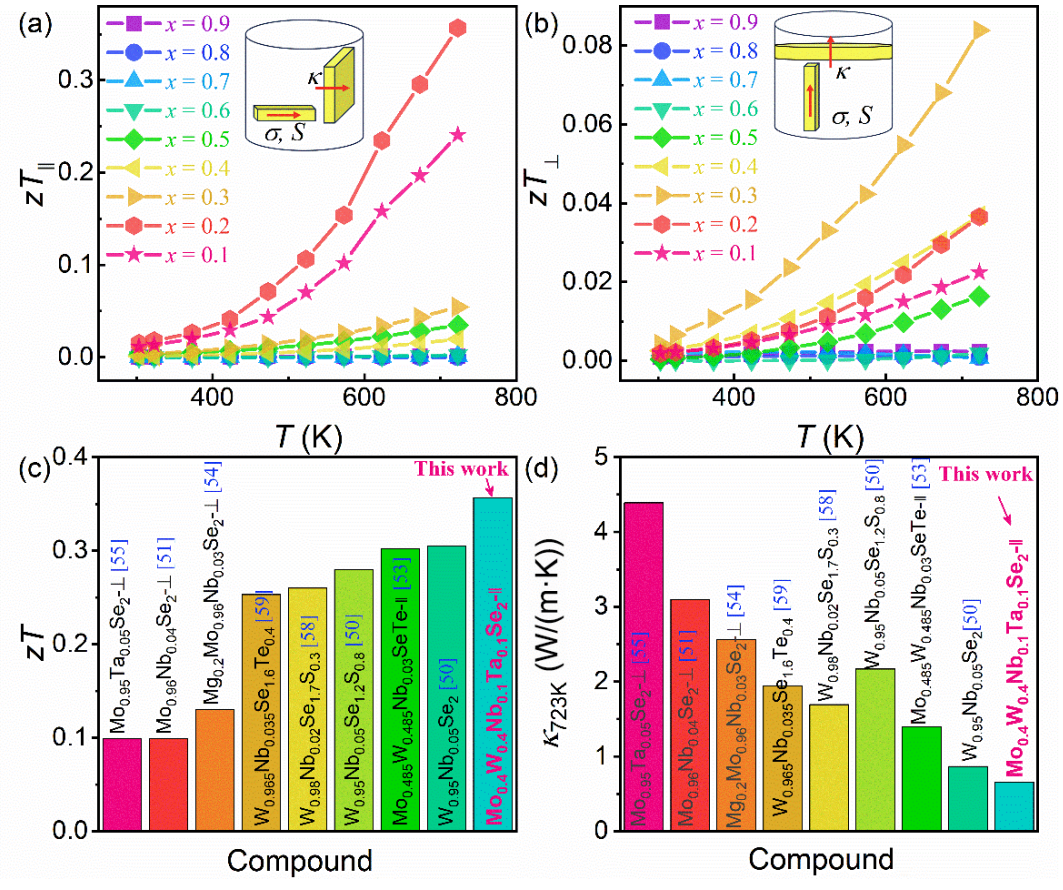

Fig. 10 Comparison of thermoelectric performances of (Mo/W)Se_2-based compounds. (a) In-plane *zT*, (b) cross-plane *zT*, (c) comparison of optimized *zT* values of (Mo/W)Se_2-based compounds, and (d) comparison of thermal conductivity of samples with optimized *zT*. Vertical and parallel paths behind chemical formula indicate cross-plane and in-plane cases, respectively.

4 Conclusions

In conclusion, we synthesized a series of high-entropy transition metal dichalcogenides with 2H and 3R polytypes, $(Mo_{0.5}W_{0.5})_{1-x}(Nb_{0.5}Ta_{0.5})_xSe_2$, $0 \le x \le 1$. A phase diagram was built by tuning the ratio between the contents of VB- and VIB- group elements and the nominal content of selenium. 2H phase was preferred with a deficient Se content, and single-phase products can be obtained when $0 \le x \le 0.6$. Moreover, excess Se caused a Se-rich atmosphere at high temperatures, improving crystallinity and facilitating the formation of 3R phases, which can be obtained in single phases when $0.3 < x \le 0.7$. With increasing *x*, the layer spacing decreased, and *a* and *V* increased. Moreover, thermodynamic calculations suggest that both 2H and 3R phases are thermodynamically favorable, and the preference for crystalline polytypes can be explained well by the difference in formation energy. Moreover, the anisotropic thermoelectric properties were characterized systematically. For NbTa-doped samples, the temperature-dependent resistivity showed metallic behavior consistent with the increase in TDOS. When $x = 0.3$, the thermal conductivity reached a minimum. With increasing *x*, the temperature dependence was reduced due to increased entropy. Furthermore, the optimized *zT* value reached 0.36@723 K when $x = 0.2$, one of the highest among (Mo/W)Se_2-based compounds. The pivotal role of thermal conductivity in thermoelectric performance was revealed, in which the high-entropy effect significantly contributed to the reduction in thermal conductivity. Our work realized a series of high-entropy layered compounds with versatile polytypes, showing improved thermoelectric properties, which also have great potential for various fields, such as catalysis, photoelectronics, and piezoelectrics.

Acknowledgements

Hongxiang Chen would like to thank Prof. Zhongzhen Luo and Prof. Huaizhou Zhao for helpful advice about their thermoelectric properties. Bing Xiao would like to thank the High-Performance Computing (HPC) Center at Xi'an Jiaotong University for computational hardware support. This work is financially supported by the Strategic Priority Research Program of the Chinese Academy of Sciences (No. XDB0470303), the National Nature Science Foundation of China (No. 52473295), the Young Elite Scientists Sponsorship Program by CAST (No. 2024QNRC001), and the State Key Laboratory of Structural Chemistry (No. 20230020).

Declaration of competing interest

The authors have no competing interests to declare that are relevant to the content of this article.

Electronic Supplementary Material

Supplementary material is available in the online version of this article at https://doi.org/10.26599/JAC.2024.9220991.

References

[1] Wang QH, Kalantar-Zadeh K, Kis A, *et al.* Electronics and optoelectronics of two-dimensional transition metal dichalcogenides. *Nat Nanotechnol* 2012, **7**: 699–712.

[2] Manzeli S, Ovchinnikov D, Pasquier D, *et al.* 2D transition metal dichalcogenides. *Nat Rev Mater* 2017, **2**: 17033.
[3] Fu Q, Han JC, Wang XJ, *et al.* 2D transition metal dichalcogenides: Design, modulation, and challenges in electrocatalysis. *Adv Mater* 2021, **33**: 1907818.
[4] Chhowalla M, Shin HS, Eda G, *et al.* The chemistry of two-dimensional layered transition metal dichalcogenide nanosheets. *Nat Chem* 2013, **5**: 263–275.
[5] Geim AK, Novoselov KS. The rise of graphene. *Nat Mater* 2007, **6**: 183–191.
[6] Ali MN, Xiong J, Flynn S, *et al.* Large, non-saturating magnetoresistance in WTe_2. *Nature* 2014, **514**: 205–208.
[7] Wu Y, Jo NH, Ochi M, *et al.* Temperature-induced Lifshitz transition in WTe_2. *Phys Rev Lett* 2015, **115**: 166602.
[8] Li P, Wen Y, He X, *et al.* Evidence for topological type-II Weyl semimetal WTe_2. *Nat Commun* 2017, **8**: 2150.
[9] Soluyanov AA, Gresch D, Wang ZJ, *et al.* Type-II Weyl semimetals. *Nature* 2015, **527**: 495–498.
[10] Wu SF, Fatemi V, Gibson QD, *et al.* Observation of the quantum spin Hall effect up to 100 Kelvin in a monolayer crystal. *Science* 2018, **359**: 76–79.
[11] Ying TP, Yu TX, Shiah YS, *et al.* High-entropy van der waals materials formed from mixed metal dichalcogenides, halides, and phosphorus trisulfides. *J Am Chem Soc* 2021, **143**: 7042–7049.
[12] Chen HX, Li S, Huang SX, *et al.* High-entropy structure design in layered transition metal dichalcogenides. *Acta Mater* 2022, **222**: 117438.
[13] Cavin J, Ahmadiparidari A, Majidi L, *et al.* 2D high-entropy transition metal dichalcogenides for carbon dioxide electrocatalysis. *Adv Mater* 2021, **33**: 2100347.
[14] Wang R, Huang JZ, Zhang XH, *et al.* Two-dimensional high-entropy metal phosphorus trichalcogenides for enhanced hydrogen evolution reaction. *ACS Nano* 2022, **16**: 3593–3603.
[15] Ying TP, Yu TX, Qi YP, *et al.* High entropy van der waals materials. *Adv Sci* 2022, **9**: 2203219.
[16] Qu J, Elgendy A, Cai RS, *et al.* A low-temperature synthetic route toward a high-entropy 2D hexernary transition metal dichalcogenide for hydrogen evolution electrocatalysis. *Adv Sci* 2023, **10**: 2204488.
[17] Zhang DL, Zeng Z, Tong QJ, *et al.* Near-unity polarization of valley-dependent second-harmonic generation in stacked TMDC layers and heterostructures at room temperature. *Adv Mater* 2020, **32**: 1908061.
[18] Suzuki R, Sakano M, Zhang YJ, *et al.* Valley-dependent spin polarization in bulk MoS_2 with broken inversion symmetry. *Nat Nanotechnol* 2014, **9**: 611–617.
[19] Zhao M, Ye ZL, Suzuki R, *et al.* Atomically phase-matched second-harmonic generation in a 2D crystal. *Light Sci Appl* 2016, **5**: 16131.
[20] Chen YL, Tian Z, Wang X, *et al.* 2D transition metal dichalcogenide with increased entropy for piezoelectric electronics. *Adv Mater* 2022, **34**: 2201630.
[21] Shi XL, Liu WD, Li M, *et al.* A solvothermal synthetic environmental design for high-performance SnSe-based thermoelectric materials. *Adv Energy Mater* 2022, **12**: 2200670.
[22] Moshwan R, Shi XL, Liu WD, *et al.* Entropy engineering: An innovative strategy for designing high-performance thermoelectric materials and devices. *Nano Today* 2024, **58**: 102475.
[23] Qin Y, Xiong T, Zhu JF, *et al.* Realizing high thermoelectric performance of Cu and Ce co-doped p-type polycrystalline SnSe via inducing nanoprecipitation arrays. *J Adv Ceram* 2022, **11**: 1671–1686.
[24] Liu ZY, Wang YG, Yang T, *et al.* Alloying engineering for thermoelectric performance enhancement in p-type skutterudites with synergistic carrier concentration optimization and thermal conductivity reduction. *J Adv Ceram* 2023, **12**: 539–552.
[25] Ao DW, Liu WD, Zheng ZH, *et al.* Assembly-free fabrication of high-performance flexible inorganic thin-film thermoelectric device prepared by a thermal diffusion. *Adv Energy Mater* 2022, **12**: 2202731.
[26] Hafner J. *Ab-initio* simulations of materials using VASP: Density-functional theory and beyond. *J Comput Chem* 2008, **29**: 2044–2078.
[27] Kresse G, Joubert D. From ultrasoft pseudopotentials to the projector augmented-wave method. *Phys Rev B* 1999, **59**: 1758–1775.
[28] Perdew JP, Burke K, Ernzerhof M. Generalized gradient approximation made simple. *Phys Rev Lett* 1996, **77**: 3865–3868.
[29] Moellmann J, Grimme S. DFT-D3 study of some molecular crystals. *J Phys Chem C* 2014, **118**: 7615–7621.
[30] Strachan J, Masters AF, Maschmeyer T. 3R-MoS_2 in review: History, status, and outlook. *ACS Appl Energy Mater* 2021, **4**: 7405–7418.
[31] Guinier A, Bokij GB, Boll-Dornberger K, *et al.* Nomenclature of polytype structures. Report of the international union of crystallography Ad-hoc Committee on the nomenclature of disordered, modulated and polytype structures. *Acta Crystall A Found Crystallogr* 1984, **40**: 399–404.
[32] Xiang HM, Xing Y, Dai FZ, *et al.* High-entropy ceramics: Present status, challenges, and a look forward. *J Adv Ceram* 2021, **10**: 385–441.
[33] Carmalt CJ, Manning TD, Parkin IP, *et al.* Formation of a new (1T) trigonal NbS_2 polytype via atmospheric pressure chemical vapour deposition. *J Mater Chem* 2004, **14**: 290–291.
[34] Witteveen C, Górnicka K, Chang J, *et al.* Polytypism and superconductivity in the NbS_2 system. *Dalton T* 2021, **50**: 3216–3223.
[35] Zhu YH, Wan B, Shen WX, *et al.* Controllable 2H/3R phase transition and conduction behavior change in $MoSe_2$:Nb substitution by high pressure synthesis for promising thermoelectric conversion. *Appl Phys Lett* 2023, **122**: 133903.
[36] Luo HX, Xie WW, Tao J, *et al.* Polytypism, polymorphism, and superconductivity in $TaSe_{2-x}Te_x$. *Proc Natl Acad Sci USA* 2015, **112**: E1174–E1180.
[37] Brixner LH, Teufer G. X-ray study and thermo-electric properties of the $W_{x/2}Mo_{x/2}Ta_{1-x}Se_2$ system. *Inorg Chem* 1963, **2**: 992–996.
[38] Brixner LH. X-ray study and thermoelectric properties of the $W_xTa_{1-x}Se_2$ system. *J Electrochem Soc* 1963, **25**: 289–293.
[39] Patil U, Caffrey NM. Composition dependence of the charge-driven phase transition in group-VI transition metal dichalcogenides. *Phys Rev B* 2019, **100**: 075424.
[40] Deng Y, Lai YM, Zhao XX, *et al.* Controlled growth of 3R phase tantalum diselenide and its enhanced superconductivity. *J Am Chem Soc* 2020, **142**: 2948–2955.
[41] Zhao XX, Ning SC, Fu W, *et al.* Differentiating polymorphs in molybdenum disulfide via electron microscopy. *Adv Mater* 2018, **30**: 1802397.
[42] Luo RC, Gao M, Wang CW, *et al.* Probing functional structures, defects, and interfaces of 2D transition metal dichalcogenides by electron microscopy. *Adv Funct Mater* 2024, **34**: 2307625.
[43] Oh JY, Lee JH, Han SW, *et al.* Chemically exfoliated transition metal dichalcogenide nanosheet-based wearable thermoelectric generators. *Energ Environ Sci* 2016, **9**: 1696–1705.
[44] Wilson JA, Yoffe AD. The transition metal dichalcogenides discussion and interpretation of the observed optical, electrical and structural properties. *Adv Phys* 1969, **18**: 193–335.
[45] Chen HX, Fu JT, Huang SX, *et al.* Realization of fine-tuning the lattice thermal conductivity and anharmonicity in layered semiconductors via entropy engineering. *Adv Mater* 2024, **36**: 2400911.
[46] Chen L, Zhang W, Lu WY, *et al.* Low thermal conductivity of dense $(TiZrHfVNbTa)C_x$ high-entropy carbides by tailoring carbon stoichiometry. *J Adv Ceram* 2023, **12**: 49–58.
[47] Wang J, Jin QQ, Song JB, *et al.* Revealing the low thermal conductivity of high-entropy rare-earth tantalates via multi-scale defect analysis. *J Adv Ceram* 2023, **12**: 2087–2100.
[48] Zheng YP, Zou MC, Zhang WY, *et al.* Electrical and thermal transport behaviours of high-entropy perovskite thermoelectric oxides. *J Adv Ceram* 2021, **10**: 377–384.

[49] Kim HS, Gibbs ZM, Tang YL, *et al.* Characterization of Lorenz number with Seebeck coefficient measurement. *APL Mater* 2015, **3**: 041506.
[50] Danish MH, Yang SH, Ming HW, *et al.* Simultaneous enhancement of the power factor and phonon blocking in Nb-doped WSe_2. *ACS Appl Mater Inter* 2023, **15**: 22167–22175.
[51] Kong S, Wu TM, Zhuang W, *et al.* Realizing p-type MoS_2 with enhanced thermoelectric performance by embedding VMo_2S_4 nanoinclusions. *J Phys Chem B* 2018, **122**: 713–720.
[52] Wang RN, Dong GY, Wang SF, *et al.* Variations of thermoelectric performance by electric fields in bilayer MX_2 (M = W, Mo; X = S, Se). *Phys Chem Chem Phys* 2017, **19**: 5797–5805.
[53] Zhang C, Li Z, Zhang M, *et al.* Synergistically improved electronic and thermal transport properties in Nb-doped $Nb_yMo_{1-y}Se_{2-2x}Te_{2x}$ solid solutions due to alloy phonon scattering and increased valley degeneracy. *ACS Appl Mater Inter* 2019, **11**: 26069–26081.
[54] Ruan LM, Zhao HZ, Li DD, *et al.* Enhancement of thermoelectric properties of molybdenum diselenide through combined Mg intercalation and Nb doping. *J Electron Mater* 2016, **45**: 2926–2934.
[55] Zhang C, Li Z, Zhang M, *et al.* Impurity states in $Mo_{1-x}M_xSe_2$ compounds doped with group VB elements and their electronic and thermal transport properties. *J Mater Chem C* 2020, **8**: 619–629.
[56] Zhou XY, Liu W, Zhang C, *et al.* Optimization of thermoelectric transport properties of Nb-doped $Mo_{1-x}W_xSeTe$ solid solutions. *J Inorg Mater* 2020, **35**: 1373–1379.
[57] Zhang C, Li Z, Zhang M, *et al.* High band degeneracy and weak chemical bonds leading to enhanced thermoelectric transport properties in 2H-$MoTe_2$. *J Solid State Chem* 2021, **300**: 122227.
[58] Yakovleva GE, Romanenko AI, Ledneva AY, *et al.* Thermoelectric properties of $W_{1-x}Nb_xSe_{2-y}S_y$ polycrystalline compounds. *J Am Ceram Soc* 2019, **102**: 6060–6067.
[59] Kriener M, Kikkawa A, Suzuki T, *et al.* Modification of electronic structure and thermoelectric properties of hole-doped tungsten dichalcogenides. *Phys Rev B* 2015, **91**: 075205.